Journal of Electron Microscopy **51(1)**: 1–9 (2002)

Full-length paper

Lipid membrane phase behaviour elucidated in real time by controlled environment atomic force microscopy

Fuyuki Tokumasu[1], Albert J. Jin[2] and James A. Dvorak[1,*]

[1]Laboratory of Parasitic Diseases, National Institute of Allergy and Infectious Diseases and [2]Division of Bioengineering and Physical Science, ORS/OD, National Institutes of Health, Bethesda, MD 20892-0425, USA
[*]To whom correspondence should be addressed. E-mail: jdvorak@niaid.nih.gov

Abstract Lipids are integral components of all biological membranes. Understanding the physical and chemical properties of these lipids is critical to our understanding of membrane functions. We developed a new atomic force microscope (AFM) approach to visualize in real time the temperature-induced lipid phase transition and domain separation processes in 1,2-dimyristoyl-*sn*-glycero-3-phosphocholine (DMPC) membranes and estimate the thermodynamics of the phase transition process. The gel and liquid crystalline phases of DMPC coexisted over a broad temperature range (~10°C). Equal partitioning into two phases occurred at a transition temperature (T_m) of 28.5°C. We developed a mathematical model to analyse AFM-derived DMPC membrane height changes as multi-peak Gaussian distributions. This approach allowed us to estimate the DMPC domain size, N, as 18–75 molecules per leaflet corresponding to a ~4.2 nm diameter circular nanodomain. Lipid nanodomains may organize into microdomains or rafts which, in concert with proteins and other lipid components, play an important dynamic role in many biomedically important processes.

Keywords atomic force microscopy, membrane, phase transition, mean-field theory, 1,2-dimyristoyl-*sn*-glycero-3-phosphocholine, thermodynamics

Received 29 May 2001, accepted 9 September 2001

Introduction

Although the overall chemical composition of cellular membranes varies, lipids play an integral role in their structure. Therefore, maintenance of the compositional integrity of these lipid components is critical to the survival of all living cells. Consequently, an understanding of the physical and chemical properties of membrane lipids is essential to our understanding of biological processes as diverse as sub-cellular transport [1–3] and invasion by infectious agents [4,5]. The physicochemical characteristics of both naturally occurring and model synthetic membrane lipids have been studied by various physical methods, including differential calorimetry [6,7], X-ray and neutron diffraction [8,9], optical microscopy [10,11], and electron microscopy [12,13]. With the advent of the atomic force microscope (AFM) [14], a new direct visualization approach to the study of membranes became possible [15,16]. For example, AFM has provided important new information on structures as diverse as synthetic membrane lipids [17–19], integral membrane proteins [20], and the knob-like protrusions on the malaria-infected erythrocyte membrane [21]. With the goal to apply the AFM to elucidate membrane phase transition processes, we developed a temperature-controlled system for the real time continuous acquisition of sequential AFM images during a linear change in temperature and a new mathematical method to quantify critical physicochemical parameters from the AFM-derived image data. As a verification of our approach, we studied the temperature-induced phase transition of 1,2-dimyristoyl-*sn*-glycero-3-phosphocholine (DMPC). We chose DMPC as it represents a class of lipids that are major components of animal cell membranes. Moreover, the physical chemistry of DMPC has been studied well by methods other than AFM and a large amount of physical data, such as T_m and ΔH, are available for DMPC. The results of this study are reported here.

Methods

Preparation of DMPC Membranes

A 0.3 % (w/v) suspension of DMPC vesicles was prepared by

hydrating powdered DMPC (SIGMA, St. Louis, MO, USA) in a 50 mM NaCl solution containing 0.3 mM NaN_3, followed by vigorous vortexing. DMPC large unilamellar vesicles (LUVs) were made with a mini-extruder (Avanti, Albaster, AL, USA) containing a 100 nm pore size Nuclepore® polycarbonate membrane (Corning, Corning, NY, USA). Extrusions were performed at 49°C until a homogeneous vesicle size was obtained (about 50 cycles). LUVs prepared by this extrusion method have been characterized to be unilamellar, of elongated shape, and of a narrow size distribution centred about the 100 nm pore diameter [22]. A 5 µl portion of a freshly prepared DMPC vesicle suspension was applied onto freshly cleaved mica, incubated for one minute to minimize multilayer membrane formation and washed with 2–3 ml of the NaCl extrusion solution [23]. Excess fluid was removed, and the sample was placed in a Multimode AFM fitted with a tapping-mode liquid cell (Digital Instruments, Santa Barbara, CA, USA), contained in an environmental chamber and equilibrated in the same NaCl solution for 10–30 min prior to imaging.

Environmental control of the atomic force microscope

A commercially available environmental chamber (Model EC12, Sun Electronic Systems, Inc., Titusville, FL, USA, Fig. 1) was modified to control the temperature of the AFM and sample. The chamber uses heaters and liquid nitrogen to maintain a set temperature. To house the MultiMode AFM, the chamber was placed on its left side and rested on silastic mounts at the four corners of the chamber which, in turn, was placed on an air table. The silastic mounts provide clearance for the AFM controller cable and ancillary chamber temperature monitoring cables. The cables were routed through an access port in the chamber wall containing a silicon plug. The rear of the chamber was fitted with a stainless steel baffle to minimize the turbulent effects of airflow through the chamber. The inside walls of the chamber were sheathed with acoustic insulation. Only two modifications to the chamber were required to make it suitable for AFM imaging. (1) The standard equipment electric fan motor and squirrel-cage fan were removed to eliminate vibration and low pressure, dry, compressed air was used to facilitate temperature equilibration. (2) The solenoid valve used to control the flow of liquid nitrogen was relocated outside of the chamber and reconnected to the chamber with a flexible, insulated delivery tube.

Chamber temperature was monitored with built-in thermocouples. Liquid nitrogen delivery and electric heaters in the chamber were controlled using the Microsoft Hyperterminal program (Microsoft, Redmond, WA, USA) and an RS-232C link between the chamber and the AFM computer. Because there is a marked temperature difference between the chamber and the AFM sample stage, the actual AFM sample temperature was monitored separately with a thermistor, (Precision 4000 Thermometer and Model 427 paediatric skin thermistor, Yellow Springs Instruments, Yellow Springs, OH, USA) bonded permanently onto the scanner stage. Heating

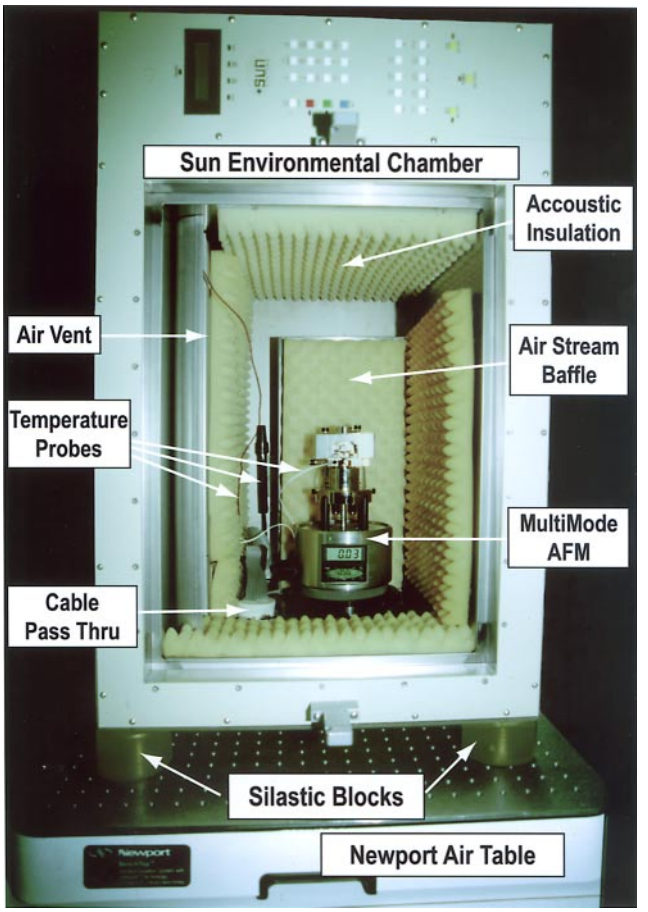

Fig. 1 View of environmentally controlled chamber containing a MultiMode AFM. The labels identify the critical components of the system.

temperature changes were maintained at a linear rate of approximately 0.14°C min^{-1} for optimum control.

Atomic force microscopy of DMPC phase transitions

All imaging was carried out in liquid Tapping Mode™ using a Nanoscope IIIa controller, a Type D scanner, and a standard silicon nitride DNP probe (Digital Instruments) with a cantilever length of 100 nm, a nominal spring constant of 0.58 N m^{-1}, and a nominal value of the tip radius of 5–20 nm. Piezo scanner calibration was performed prior to data collection by imaging a 1.8 µm pitch surface topography reference standard (Model STR2-180, VLSI Standards, Inc., San Jose, CA, USA) and tobacco mosaic virus. The overall resonance frequency of the liquid cell and probe assembly was approximately 9 kHz. Imaging was performed at a frequency of approximately 8.7 kHz. The tapping force, calculated as the ratio of engaged to free amplitude cantilever oscillations (A_{sp} / A_0) [24,25], was between 0.89 at 17°C and 0.65 at 32°C. Height- and phase-mode images were collected at 512 × 128 pixel resolution at a line scanning rate of 1.5 Hz; each image (7.7 × 1.9 µm) was collected in 1.4 min. To minimize the effects of thermal drift

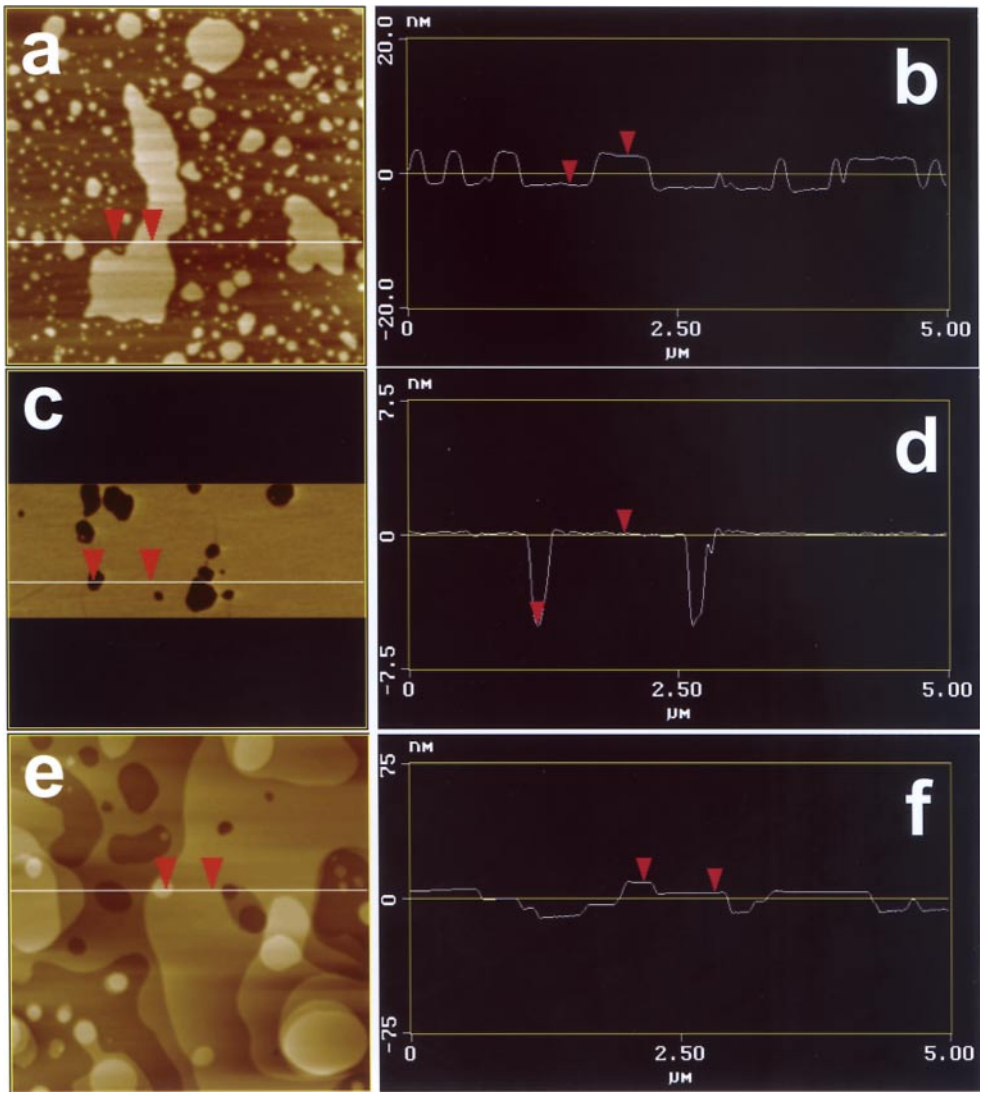

Fig. 2 DMPC vesicles can assume various forms and thicknesses depending upon incubation time at 24°C. Three types of DMPC structures on mica are shown. When the incubation time is short, vesicles appear as flat sheet-like membrane patches of various sizes (a and c). At longer incubation times, DMPC vesicles form multilayered structures (e). Cross sections at the lines shown in (a), (c), and (e), are shown in (b), (d), and (f), respectively. In (a) and (c), each layer is approximately 4–5 nm thick, corresponding to a single DMPC bilayer. In (f), there are at least 3 overlapping bilayers. The x and y distances are 5 μm for (a) and (e), and 5 × 1.25 μm for (c). The z distances are 40, 15, and 150 nm for (b), (d), and (f), respectively.

on system resonance frequency, cantilever tune was checked and adjusted between each image. Images were converted into 8-bit linear greyscale TIFF format for further analyses. Intensity and area measurements of the images were made using ImagePro® Plus version 4.1 (Media Cybernetics, Silver Spring, MD, USA). Intensity histograms at each temperature were analysed with a multi-peak Gaussian model using custom routines in Origin version 5.0 (Originlab, Northampton, MA, USA). The lipid gel phase fraction data were fitted to a mean-field model (eq. 8) using Mathcad version 8.0 (Mathsoft, Cambridge, MA, USA).

Results

DMPC membranes assume various structures on mica

A variety of DMPC membrane structures can form on mica, depending on incubation time and sample preparation conditions. The physical forces affecting the reorganization of membrane structures on mica have been described in terms of vesicular relaxation processes and interaction forces, such as hydration state and electrostatic interactions [18,23]. Figure 2 shows examples of three membrane topographies that can occur at room temperature depending upon incubation time, even when the lipid concentration and vesicle suspension volume applied on the mica are constant. After a short incubation

time (~1 min) followed by washing with NaCl solution to remove excess vesicles, DMPC vesicles can form membrane patches and flat sheets of various sizes and thicknesses (Figs 2a, 2c and 2e); marked membrane deformations and fusions also can occur. The resulting DMPC membrane can appear as patches (Fig. 2a), nearly continuous sheets (Fig. 2c) or multilayered arrays (Fig. 2e). Cross sectional analyses (Figs 2b and 2d) of Figs 2a and 2c confirm that a single 4–5 nm thick membrane layer is present on the mica. In contrast, at least 3 overlapping layers of DMPC with individual thicknesses similar to those shown in Figs 2b and 2d can occur (Fig. 2f). These data demonstrate that longer incubation times provide excess vesicles in the NaCl solution an increased opportunity to interact with the single membrane layer formed previously. We did not observe any other effects of variations in incubation time on membrane structure.

AFM detects the coexistence of two DMPC phases

DMPC membranes undergo temperature-induced phase transitions. The reported transition temperature (T_m) between the ordered gel state and disordered liquid crystalline state of DMPC ranges between 20 and 30°C in the lipid thermodynamic database (LIPIDAT) [26]. The membranes shown in Fig. 2 are in the DMPC gel phase. To directly visualize the phase transition of a fully hydrated DMPC single membrane layer, we raised the temperature from 20 to ~26°C at a heating rate of 0.11°C min^{-1} during continuous AFM scanning and recorded AFM images at three different temperatures. Figure 3 shows a 1.4 × 1.4 μm region of DMPC LUVs (a) at 23.0°C prior to the phase transition, (b) at 25.5°C during the transition process and (c) at 26.0°C at the completion of the transition process. As seen in Figs 3b and 3c, two membrane states can be identified on the basis of Gaussian decompositions. The single 4.3 nm peak present at 23.0°C (Fig. 3a) evolved at 25.5°C into two peaks with heights of 4.3 and 3.4 nm (Figs. 3b and 3c). At 26°C, the 3.4 nm peak population predominated (Fig. 3c). Although the areas contained within the two Gaussian distributions changed as a function of temperature, the membrane thicknesses, as reflected by the two Gaussian peaks, remained constant throughout the course of the phase transition. The 3.4 nm peak distribution corresponds to the liquid crystalline state; the main gel-to-liquid crystalline phase transition involves a height change of ~1 nm. Our measured heights of 3.4 nm for liquid phase and 4.3 nm for gel phase DMPC agree with the 3.6 and 4.4 nm values for the same two phases obtained by X-ray diffraction-derived measurements [27].

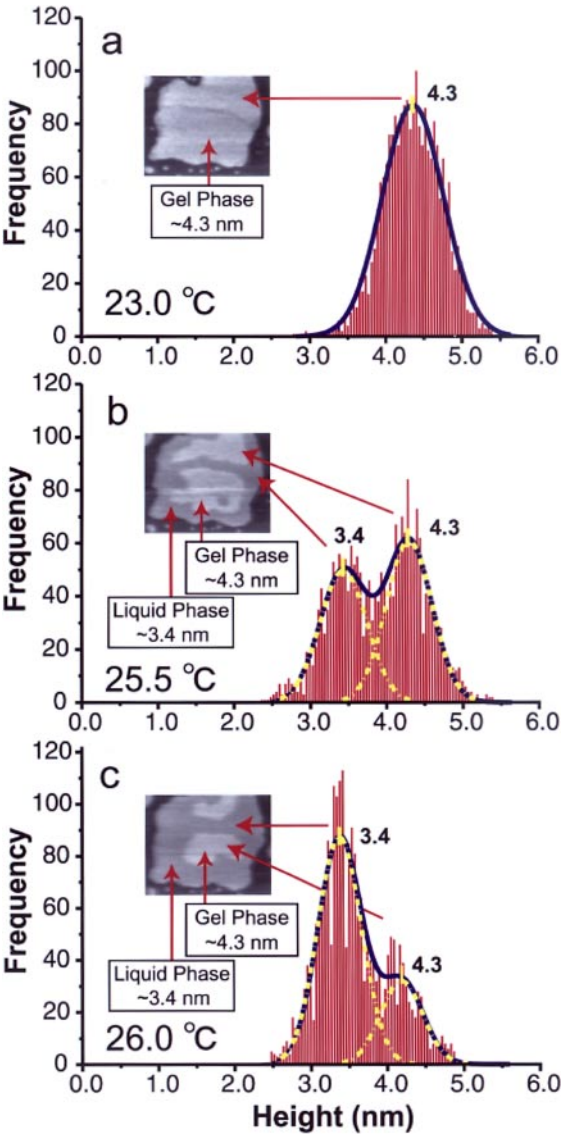

Fig. 3 AFM-derived height profiles during a temperature-induced phase transition of a DMPC membrane can be represented as Gaussian distributions. A 1.4 × 1.4 μm area was analysed from three consecutive 10 × 10 μm images collected at a heating rate of 0.11°C. (a) At 23°C, below the phase transition temperature, only a single Gaussian distribution with a peak height of 4.3 nm was present, indicating that all of the DMPC was in the gel phase. (b) At 25.5°C, two overlapping Gaussian distributions with peaks at 3.4 and 4.3 nm were present, indicating the coexistence of both gel and liquid crystalline phases. (c) At 26°C, the Gaussian distribution with a peak at 3.4 nm predominates indicating that the majority of the DMPC is in the liquid crystalline phase.

Kinetics of the temperature-induced DMPC phase transition process

To elucidate the kinetics of the phase transition process, we imaged serially fully hydrated DMPC from 17.5 to 33.0°C over a period of 2 h at a heating rate of 0.14°C min^{-1}. A representative example of the transition process is shown in Fig. 4 (arrows). The transition from gel to liquid crystalline phase began at the periphery of membrane patches and occasionally liquid crystalline phase areas were seen within gel phase islands. The transition rate is markedly temperature dependent (Fig. 5). The rate was initially slow but at the approach of T_m the phase change per temperature increment increased rapidly; the liquid crystalline phase expanded and eventually covered the entire surface at 33.0°C. We also observed mem-

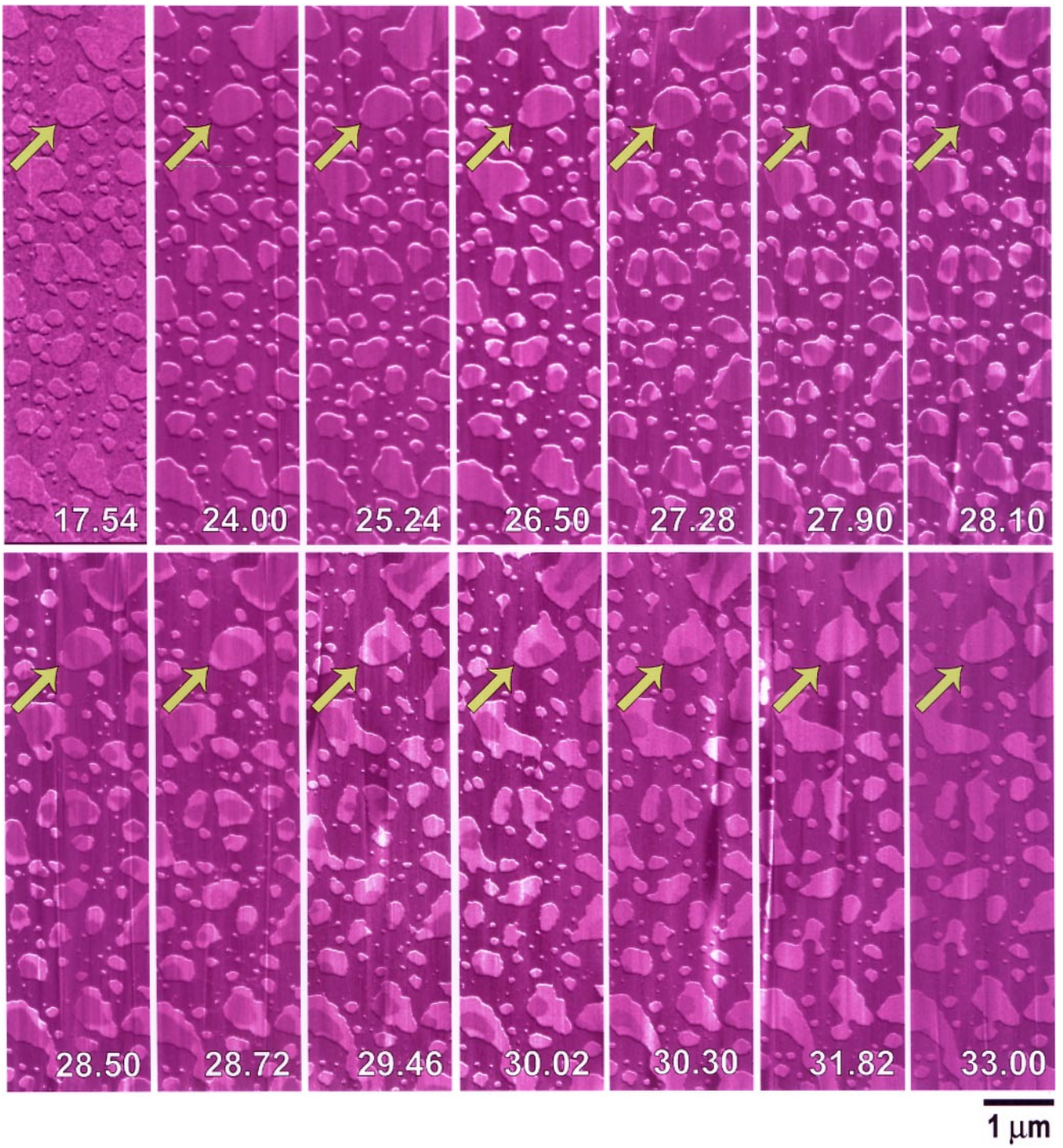

Fig. 4 Representative AFM phase-mode images depict the temperature-induced DMPC phase transition process. The light and dark regions of the images represent liquid crystalline and gel phase, respectively. The image scan size is 7.7 × 1.9 μm. The heating rate was 0.14°C min^{-1}. The arrows point to an area in the image where the complete phase transition process and membrane fusion are clearly visible. The numbers in the lower right corner of each image represent the temperature at which the image was collected. Marked structural changes began to occur gradually at 24°C; the changes occurred more rapidly at the approach to T_m at ~28.2°C. No obvious morphological changes were observed above 33°C.

brane fusions between adjacent membrane patches (c.f. Fig. 4, compare areas below arrows at 28.72 and 29.46°C). A plot of the relative gel phase versus the liquid crystalline phase areas converged at T_m ~28.2°C (Fig. 5); the phase transition was symmetrical across the T_m. The relative area change reflects changes in the temperature-induced partition ratio of the two membrane phases. Also, we observed similar phase transition features as shown in Fig. 5 at a higher heating rate (~0.2°C

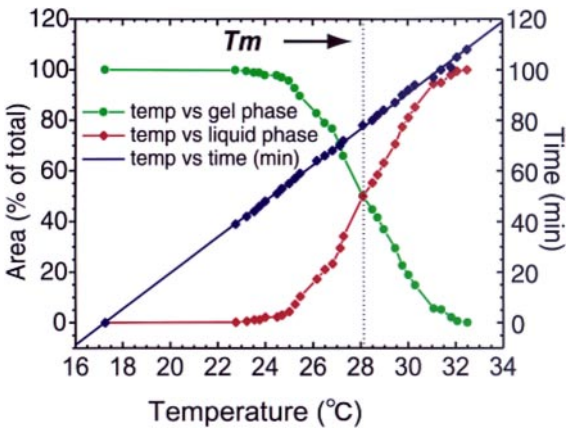

Fig. 5 Graphical representation of the temperature-induced phase transition of DMPC. The relative area of the gel phase is shown by the green symbols; the relative area of the liquid crystalline phase is shown by the red symbols. The convergence of the two data sets (vertical dotted line) represents the estimated phase transition temperature (T_m) at ~28.2°C. A plot of elapsed time versus temperature (blue symbols) demonstrates the linearity of the heating rate.

min^{-1}). If heating was stopped during the transition process, the process *per se* did not progress. Furthermore, changes in scanning force at a constant temperature did not induce phase transition (data not shown). These observations confirm that the phase transition occurs near the thermal equilibrium states; the observed phase transitions were totally temperature dependent, but insensitive to the rate at which DMPC was heated.

Figure 6 demonstrates that the above described phase transition of DMPC on mica is reversible. The DMPC sample was heated (heating rate = 0.13°C min^{-1}) and imaged continuously by AFM until a complete gel-to-liquid phase transition had occurred. The sample was then cooled (cooling rate = 0.27°C min^{-1}) and both the gel phase and non-lipid regions reappeared. Closure and opening of the membrane holes imply that the DMPC lipid surface area is greater in the liquid crystalline phase than in the gel phase, in agreement with the observed thinning of the membrane shown in Fig. 3.

The cooling rates we used were two times higher (i.e. 0.27°C min^{-1}) than the heating rates (i.e. 0.13°C min^{-1}). This difference was required to maintain a linear temperature change and stable imaging conditions over the liquid phase membrane. The hysteresis-like difference in the phase transition between the heating and cooling directions in Fig. 6 may be due to

(i) kinetic differences in the phase transition dependent upon whether the DMPC was heated or cooled,
(ii) a 'super-cooling' effect occurring in the disordered membrane phase transition, or
(iii) a loss of temperature synchrony between system and sample temperatures as a consequence of faster cooling rates.

Mean-field model yields intrinsic domain size, *N*

One remarkable new finding of our study is that the broad temperature range of the DMPC phase transition on mica is not a classical first-order phase transition process. The symmetric distribution of the gel and liquid crystalline phases around T_m rules out a simple impurity-induced pre-melting broadening as an explanation for this observation. This required that we develop a mean-field model to describe the thermodynamic characteristics as a finite-size-limited first-order transition process. As the energy associated with pressure and volume changes is negligible [28], we expand the free energy term, *f*, near the T_m for the two competing phases as

$$f_G = f_m - (N_G \cdot s_G) \cdot (T - T_m) + \cdots\cdots \quad (1)$$

and

$$f_L = f_m - (N_L \cdot s_L) \cdot (T - T_m) + \cdots\cdots \quad (2)$$

where f_m is the free energy at the T_m; N_G and N_L are the intrinsic lipid domain sizes for the gel (eq. 1) and liquid crystalline (eq. 2) phases, respectively; T_m is the phase transition temperature; and s_G and s_L are the entropy values for the gel and liquid crystalline phases, respectively. The novel assumption here is that both the gel and liquid crystalline phase domains exhibit intrinsic excitations (e.g. lipid acyl chain length fluctuations [19]) of finite size. Making a further simplification that $N_G \cong N_L \cong N$, where *N* is the intrinsic lipid domain size at T_m, the free energy difference for the lipid domain in the two respective phases is

$$\Delta f = f_G - f_L \cong (s_L - s_G) \cdot (T - T_m) \cdot N \quad (3)$$

Because the pressure–volume associated energy term is negligible, we obtain the thermodynamic relationship

$$\Delta H \cong N_A \cdot (s_L - s_G) \cdot T_m \quad (4)$$

where ΔH is the enthalpy required for the phase transition and N_A is Avogadro's number. Therefore,

$$\Delta f = (s_L - s_G) \cdot (T - T_m) \cdot N = \Delta H \cdot N \cdot (T - T_m)/N_A \cdot T_m \quad (5)$$

Thermal equilibrium is valid for the distribution of the phases observed by AFM. Thus, the probability functions, P_G for the gel phase and P_L for the liquid crystalline phase, can be expressed as

$$P_G \propto e^{-f_G/k_B T} \propto e^{-f_G/k_B T_m},\ P_L \propto e^{-f_L/k_B T} \propto e^{-f_L/k_B T_m} \quad (6)$$

where k_B is the Boltzmann constant and $T \cong T_m$ is expressed in K (kelvin).

Thus, the lipid fraction occupied by the gel phase domain is

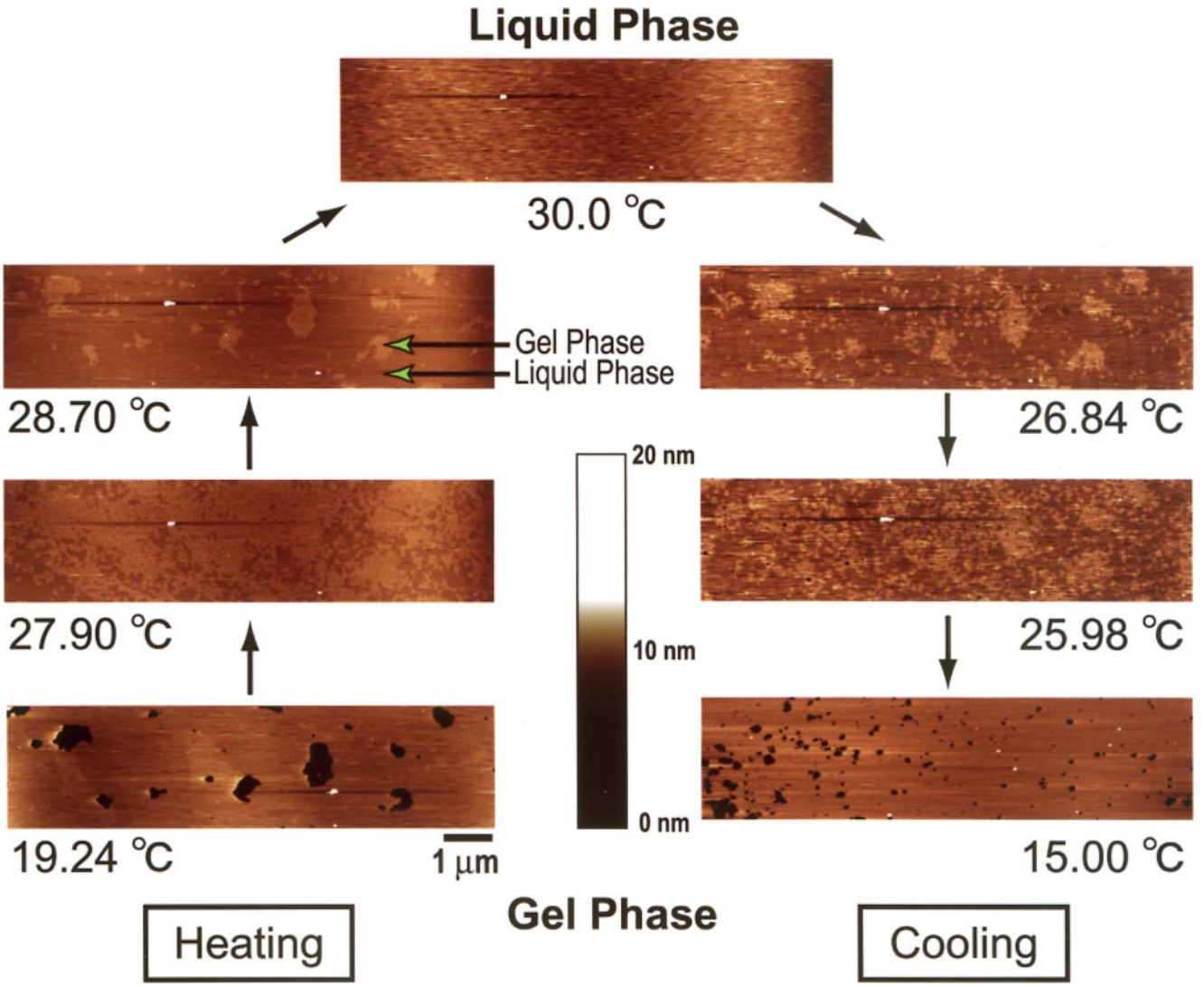

Fig. 6 The temperature-induced phase transition of DMPC is reversible. A DMPC membrane was heated from the gel phase at 19°C to the complete liquid crystalline phase at 30°C and subsequently cooled to 15°C. The DMPC returned to the gel phase. The disappearance and reappearance of non-lipid regions correspond to changes in lipid surface areas associated with hydrophobic acyl chain interactions.

$$\rho_G = \frac{P_G}{P_G + P_L} = \frac{1}{1 + e^{(f_G - f_L)/k_B T}} \tag{7}$$

where ρ_G is the gel phase fraction. Substituting eq. 5 results in

$$\rho_G = 1 \Big/ \left(1 + e^{\frac{\Delta H \cdot N \cdot (T - T_m)}{R \cdot T_m^2}} \right) \tag{8}$$

where the gas constant $R = N_A \cdot k_B$.

The above mathematical treatment closely models the observed DMPC membrane phase behaviour on a flat mica substrate, as shown in Fig. 4. In our analyses we measured both the total area ratio and the membrane thickness ratio of the two coexisting DMPC phases to yield the gel phase fractions at each temperature using

$$\rho_G = \frac{A_G/a_G}{A_G/a_G + A_L/a_L} \cong \frac{1}{1 + (A_L/A_G) \cdot (h_L/h_G)} \tag{9}$$

where the incompressibility of volume (= height × area) per lipid, $h_G \cdot a_G \cong h_L \cdot a_L$, can be used together with the measured gel/liquid crystalline area ratio, A_G / A_L, and the height ratio, h_G / h_L. A comparison of this theoretical model (eq. 8) and actual data clearly demonstrates a close correspondence (Fig. 7). Moreover, the fitting process yields the critical parameter for system enthalpy, $\Delta H \cdot N = 150$ kcal mol^{-1} per domain, and the estimated $T_m = 28.5$°C. The enthalpy value, ΔH, for the DMPC phase transition is relatively constant over a 2–8 kcal mol^{-1} range, reflecting the difference in the degrees of freedom of the lipid chains in the two states and allows us to estimate that the DMPC intrinsic domain size, N, is 18–75 lipid molecules per leaflet. As surface area per DMPC molecule is ~60 Å^2 [28] and the area per lipid domain is ~1380 Å^2 when $\overline{N}/2 = 23$ lipid molecules per leaflet, the domain diameter (d) is $2 \cdot (13.8 / \pi)^{1/2}$ nm ≅ 4.2 nm.

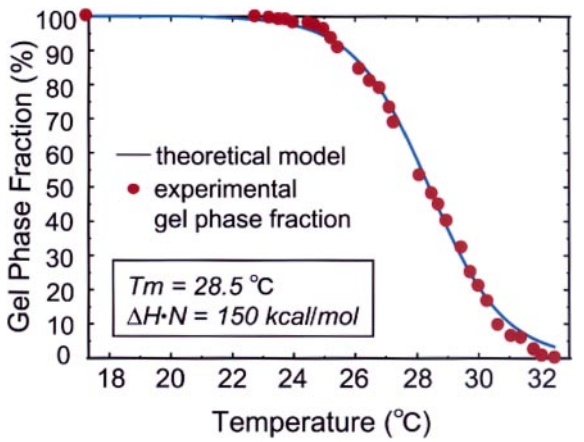

Fig. 7 Graphical demonstration of the use of AFM data to estimate the thermodynamic parameters of the temperature-induced phase transition of DMPC. Equation 8 was used to estimate the system enthalpy ($\Delta H \cdot N$). The red symbols represent the measured values of the gel phase fraction obtained from eq. 9. The solid line represents the theoretical fit of the data using eq. 8. The transition temperature (T_m) and enthalpy ($\Delta H \cdot N$) are 28.5°C and 150 kcal mol^{-1}, respectively.

Discussion

We developed an environmental-control system for real time AFM studies of temperature-dependent phase transitions of biological membranes and verified the utility of the system using DMPC. The advantages of our system are that we can detect in real time domain transformations and the coexistence of phase complexes during the phase transition process. While the coexistence of DMPC membrane phases at distinct, static temperatures have been reported [19,29], our ability to continuously collect serial AFM liquid tapping-mode data over a large temperature range at a ~0.1°C min^{-1} heating rate allows, in concert with our new mean-field model, a more extensive and dynamic classical thermodynamic analyses of the entire transition process.

We demonstrated for the first time that phase transitions in both heating and cooling directions occur on a mica substrate and that the AFM is an excellent tool to estimate critical physico-chemical parameters of the transition process. We found that the transition process is unexpectedly broad with the prolonged coexistence of two lipid phase domains. In addition, we observed a higher transition temperature than the mode, the most frequent value of T_m of DMPC (~24°C) obtained by differential scanning calorimetry (DSC) studies. Historically, phase behaviour of lipid vesicle membranes has been studied in physically unrestricted free space systems such as solutions. However, it is probable that the confinement of lipid membranes to a substrate alters their phase behaviour [30,31], as there are additional interaction forces imposed by the spatial confinement on a two-dimensionally flat mica surface. Mica–membrane interactions would tend to suppress membrane undulations and favour a more ordered gel phase, resulting in a higher phase transition temperature. Within a single membrane, lateral variations in the phase transition also exist (Fig. 6). We believe that local non-uniformities, such as charge density, of the mica surface could slightly shift the phase transition temperature. This confinement of the membrane better describes the phase behaviour of cell membranes in more physiologically normal environments where they physically interact with other cells and extracellular matrices. Our mean-field model takes these factors into consideration by focusing on a finite-sized cooperative unit in the lipid membrane and accurately estimates its size using the AFM. Our real time AFM data demonstrate that the DMPC intrinsic domain size, N, is 18–75 lipid molecules per leaflet corresponding to a domain diameter (d) of 4.2 nm. This surprisingly small domain size may represent the unit size for lateral cooperativity of lipid molecules, which form the larger domain clusters reported here by AFM.

Biological membranes demonstrate marked qualitative and quantitative differences in both lipid and protein components. This results in complex variations in their thermodynamic properties and, consequently, particular patterns of phase-domain formation [32,33]. Membrane phase transitions and phase-domain formations play an important role in controlling membrane-related events, such as the rates of macromolecular reactions, invaginations and fusions of vesicles as well as providing the microenvironment for certain membrane proteins [34,35]. A practical example of the possible implications of our work concerns the infectious process. In infectious diseases, invasion is often accompanied by marked perturbations and deformations of the host cell membrane [4]. Understanding these phenomena is critically important to interdiction of the infectious process. It is probable that lipid phase-domain formations in concert with clusters of particular membrane proteins form morphologically unique structures (e.g. membrane rafts) that can be utilized by infectious agents. Our AFM-based, real time visualization and thermodynamic analysis of membrane phase transitions reported here represent a new approach to better understand membrane-associated molecular and cellular events, not only in infectious diseases but in many other biomedically important processes as well.

Concluding remarks

We have developed a new real time AFM method and unique mathematical approach to visualize temperature-induced membrane transitions and quantify the thermodynamic parameters of the process. We verified the applicability of our approach using the lipid, 1,2-dimyristoyl-*sn*-glycero-3-phosphocholine (DMPC). This approach should be widely useful to better understand complex membrane-associated molecular and cellular events in many biomedically important processes.

Acknowledgements

F. Tokumasu is a Japan Society for the Promotion of Science Research Fellow in Biomedical and Behavioural Research at National Institutes of Health, Bethesda, Maryland, USA.

References

1 Futerman A H, Ghidoni R, and van Meer G (1998) Lipids: regulatory functions in membrane traffic and cell development. *EMBO J.* **17**: 6772–6775.

2 Mukherjee S, Ghosh R N, and Maxfield F R (1997) Endocytosis. *Physiol. Rev.* **77**: 759–803.

3 Moffett S, Brown D A, and Linder M E (2000) Lipid-dependent targeting of G proteins into rafts. *J. Biol. Chem.* **275**: 2191–3166.

4 Dvorak J A, Miller L H, Whitehouse W C, and Shiroishi T (1975) Invasion of erythrocytes by malaria merozoites. *Science* **187**: 748–750.

5 Shogomori H and Futerman A H (2000) Cholera toxin is found in detergent-insoluble rafts/domains at the cell surface of hippocampal neurons but is internalized via a raft-independent mechanism. *J. Biol. Chem.* **276**: 9182–9188.

6 Huang C and Li S (1999) Calorimetric and molecular mechanics studies of the thermotropic phase behavior of membrane phospholipids. *Biochim. Biophys. Acta* **1422**: 273–307.

7 Maggio B, Fidelio G D, Cumar F A, and Yu R K (1986) Molecular interactions and thermotropic behavior of glycosphingolipids in model membrane systems. *Chem. Phys. Lipids* **42**: 49–63.

8 Bedzyk M J, Bilderback D H, Bommarito G M, Caffrey M, and Schildkraut J S (1988) X-ray standing waves: a molecular yardstick for biological membranes. *Science* **241**: 1788–1791.

9 Koenig B W, Krueger S, Orts W J, Majkrzak C F, Berk N F, Silverton J V, and Gawrisch K (1996) Neutron reflectivity and atomic force microscopy studies of a lipid bilayer in water adsorbed to the surface of a silicon single crystal. *Langmuir* **12**: 1343–1350.

10 Korlach J, Schwille P, Webb W W, and Feigenson G W (1999) Characterization of lipid bilayer phases by confocal microscopy and fluorescence correlation spectroscopy. *Proc. Natl. Acad. Sci. USA* **96**: 8461–8466.

11 Hwang J, Tamm L K, Bohm C, Ramalingam T S, Betzig E, and Edidin M (1995) Nanoscale complexity of phospholipid monolayers investigated by near-field scanning optical microscopy. *Science* **270**: 610–614.

12 Borovyagin V L and Sabelnikov A G (1989) Lipid polymorphism of model and cellular membranes as revealed by electron microscopy. *Electron Microsc. Rev.* **2**: 75–115.

13 Cullis P R, Hope M J, and Tilcock C P (1986) Lipid polymorphism and the roles of lipids in membranes. *Chem. Phys. Lipids* **40**: 127–144.

14 Binning G and Quate C F (1986) Atomic force microscope. *Phys. Rev. Lett.* **56**: 930–933.

15 Shao Z, Mou J, Czajkowksy D M, Yang J, and Yuan J Y (1996) Biological atomic force microscopy: what is achieved & what is needed. *Adv. Phys.* **45**: 1–86.

16 Lal R and John S A (1994) Biological applications of atomic force microscopy. *Am. J. Physiol.* **266**: C1–C21.

17 Dufrene Y F, Boland T, Schneider J W, Barger W R, and Lee G U (1998) Characterization of the physical properties of model biomembranes at the nanometer scale with the atomic force microscope. *Faraday Discuss.* 79–94.

18 Muresan A S and Lee K Y C (2001) Shape evolution of lipid bilayer patches adsorbed on mica: an atomic force microscopy study. *J. Phys. Chem. B* **105**: 852–855.

19 Nielsen L K, Bjornholm T, and Mouritsen O G (2000) Fluctuations caught in the act. *Nature* **404**: 352.

20 Takeyasu K, Omote H, Nettikadan S, Tokumasu F, Iwamoto-Kihara A, and Futai M (1996) Molecular imaging of *Escherichia coli* F0F1-ATPase in reconstituted membranes using atomic force microscopy. *FEBS Lett.* **392**: 110–113.

21 Nagao E, Kaneko O, and Dvorak J A (2000) *Plasmodium falciparum*-infected erythrocytes: qualitative and quantitative analyses of parasite-induced knobs by atomic force microscopy. *J. Struct. Biol.* **130**: 34–44.

22 Jin A J, Huster D, Gawrisch K, and Nossal R (1999) Light scattering characterization of extruded lipid vesicles. *Eur. Biophys. J.* **28**: 187–199.

23 Egawa H and Furusawa K (1999) Liposome adhesion on mica surface studied by atomic force microscopy. *Langmuir* **15**: 1660–1666.

24 Magonov S N, Elings V, and Whangbo M-H (1997) Phase imaging and stiffness in tapping-mode atomic force microscopy. *Sur. Sci. Lett.* **375**: L385–L391.

25 Nagao E and Dvorak J A (1999) Phase imaging by atomic force microscopy: analysis of living homoiothermic vertebrate cells. *Biophys. J.* **76**: 3289–3297.

26 Caffrey M and Hogan J (1992) LIPIDAT: a database of lipid phase transition temperatures and enthalpy changes. DMPC data subset analysis. *Chem. Phys. Lipids* **61**: 1–109.

27 Janiak M J, Small D M, and Shipley G G (1976) Nature of the thermal pretransition of synthetic phospholipids: dimyristolyl- and dipalmitoyllecithin. *Biochemistry* **15**: 4575–4580.

28 Dammann B, Fogedby H C, Ipsen J H, Jeppesen C, Jorgensen K, Mouritsen O G, Risbo M, Sabra M C, Sperotto M M, and Zuckermann M J (1996) Computer simulation of the thermodynamic and comformational properties of liposomes. In: *Handbook of Nonmedical Applications of Liposomes*, eds Lasic D D and Barenholz Y, pp. 85–127, (CRC Press, Inc., Boca Raton).

29 Giocondi M C, Pacheco L, Milhiet P E, and Le Grimellec C (2001) Temperature dependence of the topology of supported dimirystoyl-distearoyl phosphatidylcholine bilayers. *Ultramicroscopy* **86**: 151–157.

30 Jin A J, Bjurstrom M R, and Chan M H (1989) Thermodynamic evidence of first-order melting of Xe on graphite. *Phys. Rev. Lett.* **62**: 1372–1375.

31 Fisher M E and Jin A J (1992) Is short-range 'critical' wetting a first-order transition? *Phys. Rev Lett.* **69**: 792–795.

32 Brown D A and London E (2000) Structure and function of sphingolipid- and cholesterol-rich membrane rafts. *J. Biol. Chem.* **275**: 17221–17224.

33 Simons K and Toomre D (2000) Lipid rafts and signal transduction. *Nat. Rev. Mol. Cell. Biol.* **1**: 31–39.

34 Jacobson K, Sheets E D, and Simson R (1995) Revisiting the fluid mosaic model of membranes. *Science* **268**: 1441–1442.

35 Edidin M (1997) Lipid microdomains in cell surface membranes. *Curr. Opin. Struct. Biol.* **7**: 528–532.